ADVANCED MATERIALS
www.advmat.de

Giant Hall Switching by Surface-State-Mediated Spin-Orbit Torque in a Hard Ferromagnetic Topological Insulator

*Lixuan Tai, Haoran He, Su Kong Chong, Huairuo Zhang, Hanshen Huang, Gang Qiu, Yuxing Ren, Yaochen Li, Hung-Yu Yang, Ting-Hsun Yang, Xiang Dong, Bingqian Dai, Tao Qu, Qingyuan Shu, Quanjun Pan, Peng Zhang, Fei Xue, Jie Li, Albert V. Davydov, and Kang L. Wang**

Topological insulators (TI) and magnetic topological insulators (MTI) can apply highly efficient spin-orbit torque (SOT) and manipulate the magnetization with their unique topological surface states (TSS) with ultrahigh efficiency. Here, efficient SOT switching of a hard MTI, V-doped $(Bi,Sb)_2Te_3$ (VBST), with a large coercive field that can prevent the influence of an external magnetic field, is demonstrated. A giant switched anomalous Hall resistance of 9.2 kΩ is realized, among the largest of all SOT systems, which makes the Hall channel a good readout and eliminates the need to fabricate complicated magnetic tunnel junction (MTJ) structures. The SOT switching current density can be reduced to 2.8×10^5 A cm^{-2}, indicating its high efficiency. Moreover, as the Fermi level is moved away from the Dirac point by both gate and composition tuning, VBST exhibits a transition from edge-state-mediated to surface-state-mediated transport, thus enhancing the SOT effective field to $(1.56 \pm 0.12) \times 10^{-6}$ T A^{-1} cm^2 and the interfacial charge-to-spin conversion efficiency to 3.9 ± 0.3 nm^{-1}. The findings establish VBST as an extraordinary candidate for energy-efficient magnetic memory devices.

1. Introduction

Spin-orbit torque (SOT) uses relativistic spin-orbit interaction in heavy elements to convert charge current to spin current and manipulate the magnetization.[1] Heavy elements are usually placed adjacent to magnetic materials and generate a spin current via mechanisms such as spin Hall effect[2–6] or Rashba–Edelstein effect[7–9] to exert spin–orbit torque (SOT) and switch the magnets. As a writing method for magnetoresistive random access memories (MRAM), SOT has great advantages of low writing current and high reliability, so it has promising applications in high-efficiency nonvolatile memory.[10–12]

Current-induced SOT switching was first demonstrated in heavy metal/ferromagnet (HMFM) bilayer heterostructures, where the heavy metal acts as a SOT source material.[5,6,13,14] The material choices for SOT sources have been extended to various quantum and 2D materials, such as the Weyl semimetal WTe_2.[15,16]

Compared with these conducting materials, topological insulators (TI) are more advantageous as SOT source materials because their insulating bulk and conducting spin-polarized surface states can enable much higher SOT efficiency.[17–20] In TI, the spin-orbit coupling is large enough to invert the band structure and create unique topological surface states (TSS), represented by a linearly dispersed Dirac cone in the band structure. These TSSs are spin-polarized and have spin-momentum locking, meaning the spin polarization uniquely depends on the momentum.[21–26] Various techniques have been developed to determine the SOT efficiency in TI, including spin-torque ferromagnetic resonance,[17,20,27,28] spin pumping,[29–31] magneto-optical Kerr effect,[32,33] loop shift method in transport,[32,34] and second harmonic measurements in transport.[18,19,33,35,36] The SOT efficiency can be quantified by the spin Hall angle θ_{SH}, which is defined as the ratio between spin current density J_S and electric current density J_C, or $\theta_{SH} = J_S / J_C$, and TI's spin Hall angle is reported to be as large as 140 at 1.9 K[18,19] and around 1–3 at room temperature,[28,35,36] although the spin Hall angle only applies to the 3D bulk origin of SOT (like the spin Hall effect) and might not be physically meaningful.[20,30] So far, SOT has

L. Tai, H. He, S. K. Chong, H. Huang, G. Qiu, Y. Ren, Y. Li, H.-Y. Yang, T.-H. Yang, X. Dong, B. Dai, T. Qu, Q. Shu, Q. Pan, P. Zhang, K. L. Wang
Department of Electrical and Computer Engineering
University of California
Los Angeles, CA 90095, USA
E-mail: wang@ee.ucla.edu
H. Zhang
Theiss Research
Inc.
La Jolla
CA 92037, USA
H. Zhang, A. V. Davydov
Materials Science and Engineering Division
National Institute of Standards and Technology (NIST)
Gaithersburg, MD 20899, USA
F. Xue
Department of Physics
University of Alabama at Birmingham
Birmingham, AL 35294, USA
J. Li
School of Materials Science and Engineering
Shanghai University
Shanghai 200444, China
The ORCID identification number(s) for the author(s) of this article can be found under https://doi.org/10.1002/adma.202406772

DOI: 10.1002/adma.202406772

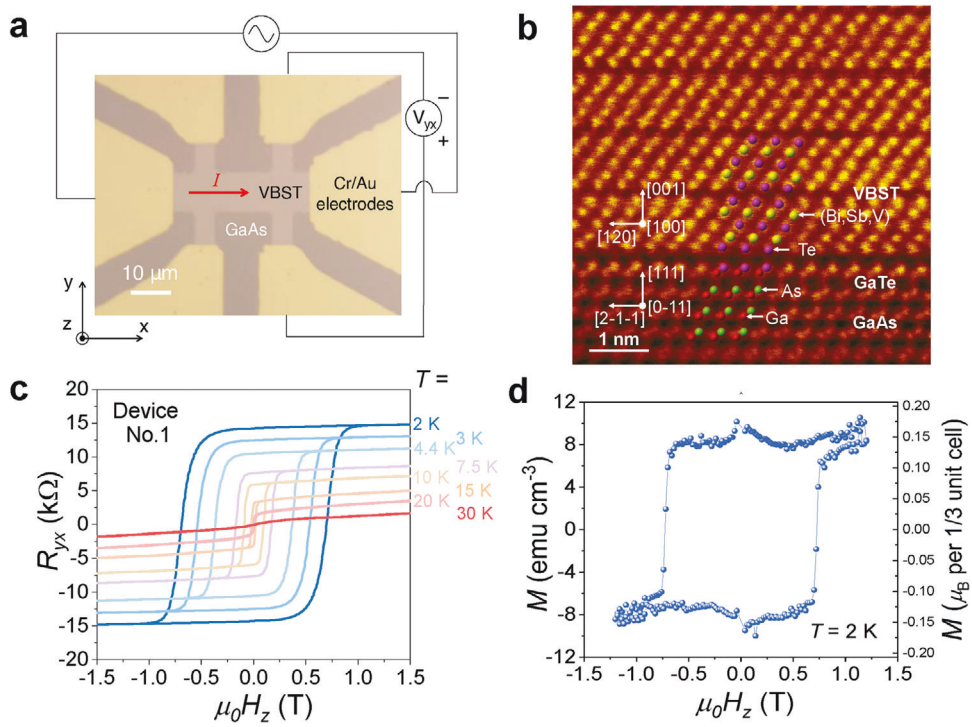

Figure 1. Experimental set-up and the magnetic properties of the V-doped $(Bi,Sb)_2Te_3$ (VBST) films. a) Optical micrograph of the Hall bar device. b) A cross-sectional high-angle annular dark-field scanning transmission electron microscopy (HAADF–STEM) image of the VBST film on the GaAs substrate. c) Anomalous Hall resistance R_{yx} as a function of an external out-of-plane magnetic field H_z at various temperatures in Device No. 1. d) Magnetization M as a function of an external out-of-plane magnetic field H_z at $T = 2$ K.

been explored in various TI/non-TI magnet bilayers for efficient current-induced magnetization switching.[28,33–40]

Another approach to utilizing the highly efficient SOT of TI is using its magnetic counterparts, the magnetic topological insulators (MTI). MTI is more advantageous than TI/non-TI magnet bilayers because it does not need another heterogeneous magnetic layer for magnetization switching and is thus free from problems with the bilayer interface and shunting in the metallic ferromagnetic layer. By doping TI with magnetic ions such as Cr, Mn, or V, ferromagnetism can be established within TI itself. A gap can be opened at the crossing point of the Dirac cone, the Dirac point, leaving pure edge state transport only and thus hosting the quantum anomalous Hall effect (QAHE).[41–45] Therefore, MTI or TI/MTI bilayer has reached one of the highest SOT efficiency ever reported.[18,19,32,46]

Among all the various MTIs, V-doped $(Bi,Sb)_2Te_3$ (VBST) is unique because it is a hard ferromagnetic TI with a larger coercive field (>0.5 T, one order of magnitude larger than its Cr-doped counterparts), thus making it robust against the influences of external magnetic fields. Thanks to its robust ferromagnetism, it also exhibits spontaneous magnetization (and QAHE) without the need for magnetic field training or field cooling, in contrast to its Cr-doped counterparts.[45] All these unique properties of VBST as a hard ferromagnetic TI make it an attractive candidate for spintronics applications.

Here, we demonstrate efficient current-driven magnetization switching of a hard ferromagnetic TI, V-doped $(Bi,Sb)_2Te_3$ (VBST) by its surface-state-mediated SOT. A giant switched anomalous Hall resistance, a low switching current density, or a high switching ratio can be realized. By analyzing the second-harmonic signals of the anomalous Hall resistance, we calibrate the efficiency of the SOT, showing a high effective field to current ratio, which is three orders of magnitude larger than those reported in HMFMs. More interestingly, Fermi level dependence by tuning the gate voltage or the material composition reveals that as the surface state transport replaces edge state transport, more carriers from the surface states significantly enhance SOT. This hard ferromagnetism, giant Hall switching, and efficient surface-state-mediated SOT in VBST provide a perfect platform for energy-efficient magnetic memory devices.

2. Material Characterizations and Device Structure

Figure 1a shows the Hall bar device structure with schematic illustrations of the experimental set-up, where the bright region shows the Hall bar of the V-doped $(Bi,Sb)_2Te_3$ (VBST) thin film, the dark region shows the semi-insulating GaAs (111)B substrate and the gold region is the Cr/Au electrodes. The length and width of the Hall bar are 20 and 10 μm, respectively. All devices (Device No. 1–8) in this work have the same Hall bar geometry, and only Device No. 3 has an additional top gate.

In order to study the crystalline quality of the thin film, cross-sectional atomic-resolution HAADF–STEM (high-angle annular dark-field scanning transmission electron microscopy) was carried out. The captured cross-sectional image of the VBST sample, as presented in Figure 1b, shows that the quintuple layer (QL) structure of the epitaxial rhombic VBST film and van der Waals gaps between every two QLs, indicating high crystalline

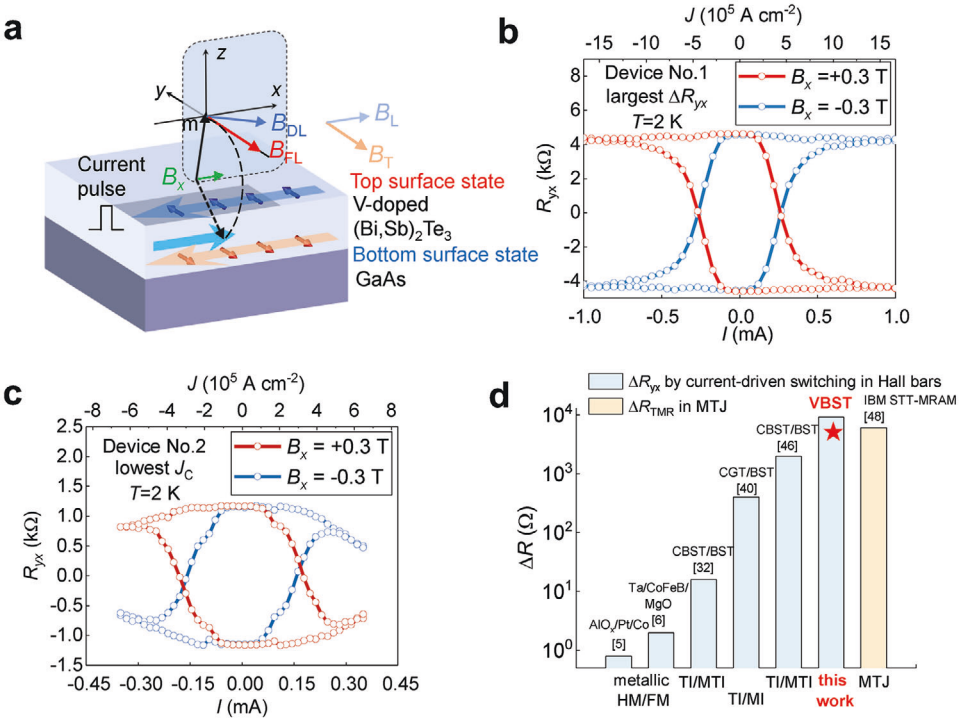

Figure 2. Current-induced switching of magnetization in V-doped $(Bi,Sb)_2Te_3$ (VBST). a) Schematic illustration of current-induced magnetization switching with damping-like (DL) and field-like (FL) spin-orbit torque (SOT) effective fields B_{DL} and B_{FL}. B_L or B_T is an applied external longitudinal or transverse magnetic field for Figure 3. b,c) The Hall resistance R_{yx} after applying each writing pulse as a function of the pulse amplitude I as well as the current density J, taken in b) Device No. 1 and c) Device No. 2, with an in-plane assisting magnetic field B_x of ±0.3 T. All measurements were carried out at T = 2 K. d) Comparison between the switched resistances by current in various schemes.

quality. The image also reveals an atomically sharp interface between the VBST and the Te-terminated GaAs (111)B substrate from the Te-rich pre-annealing process to remove the top oxide layer. In conclusion, the cross-sectional STEM image confirms the high crystalline quality of VBST.

For the transport properties of VBST samples, the Hall resistance is presented in Figure 1c as a function of an external out-of-plane magnetic field H_z at various temperatures on a 6 QL $V_{0.14}(Bi_{0.27}Sb_{0.73})_{1.86}Te_3$ Hall bar (Device No. 1). A wide hysteresis loop from the anomalous Hall effect (AHE) with a large coercive field of 0.7 T is observed at T = 2 K, one order of magnitude larger than its Cr-doped counterparts, indicating the nature of VBST as a hard ferromagnet. The sample also exhibits a large anomalous Hall resistance of 14.8 kΩ at T = 2 K. The anomalous Hall resistance and coercive field shrinks at higher temperatures, and the AHE persists up to 30 K.

In Figure 1d, the magnetization M of VBST as a function of an external out-of-plane magnetic field H_z at T = 2 K, from which the diamagnetic background has been removed, also reveal a large coercive field of 0.7 T and a small saturation magnetization of M_S = 8.3 emu cm^{-3}, which corresponds to a net magnetic moment of 0.15μ_B (μ_B is Bohr magneton) per 1/3 unit cell (5 atoms of $(Bi,Sb)_2Te_3$ included).

VBST's unique magnetic properties make it an ideal candidate for spintronics materials. Its large coercive field, which is more than one order of magnitude larger than typical ferromagnets, can prevent the influence of an external magnetic field and make the magnetic storage robust against external magnetic perturbations. Its small saturation magnetization, which is two orders of magnitude smaller than typical ferromagnets, makes the stray field small and eliminates unwanted magnetic crosstalk between neighboring devices.

3. Current-Induced Spin-Orbit Torque Switching

Current-driven SOT switching of magnetization was performed in the hard ferromagnetic TI VBST. **Figure 2a** shows a schematic illustration of surface-state-mediated SOT switching in VBST. When a current is injected into the + **x** direction, electrons will move into the − **x** direction through the top and bottom surface states that carry + **y** and − **y** spin polarizations, respectively, from the spin-momentum locking mechanism of TIs. Although the top and bottom surface states carry opposite spin directions so their contributions to the SOT cancel each other, the structural asymmetry in the VBST/GaAs structure can induce different interfacial properties and different top and bottom surface state carrier densities, thus leading to net current-induced SOT.[19,47] The spin accumulation exerts torques on the magnetization **m**, thus leading to its flipping. The SOT can be decomposed into two parts, namely the field-like (FL) and damping-like (DL) torques, as in Equation (1).[1]

$$\boldsymbol{T} = \boldsymbol{M} \times \left(\boldsymbol{B}_{FL} + \boldsymbol{B}_{DL}\right) = -M_S \left[B_{FL}\mathbf{m} \times \boldsymbol{\zeta} + B_{DL}\boldsymbol{m} \times (\boldsymbol{m} \times \boldsymbol{\zeta})\right] (1)$$

here, $\mathbf{B}_{FL} = B_{FL}\,\boldsymbol{\zeta}$ and $\mathbf{B}_{DL} = B_{DL}\,\mathbf{m} \times \boldsymbol{\zeta}$ represent the FL and DL effective fields, $\mathbf{m} = \mathbf{M}/M_S$ is the magnetization unit vector, **M**

is the magnetization, M_S is the saturation magnetization, and $\boldsymbol{\zeta}$ is the unit vector of the net SOT spin polarization. The FL torque produces the precession of the magnetization, and the DL torque produces the damping of the magnetization toward its equilibrium state, thus mainly contributing to the switching. Therefore, the DL torque is usually used to evaluate the SOT efficiency. For deterministic switching, an in-plane external assisting magnetic field B_x is needed to drive **m** toward **x** direction and gives $\mathbf{B}_{DL}$ a necessary **z** component to flip the magnetization.

The measurement scheme of current-induced switching is by applying a series of current pulses and outlined in Section S5 (Supporting Information). Figure 2b presents the Hall resistance R_{yx} of Device No. 1, 6 QL $V_{0.14}(Bi_{0.27}Sb_{0.73})_{1.86}Te_3$ as a function of the writing pulse amplitude I and the current density J, when $B_x = \pm 0.3$ T. All measurements were carried out at the ambient temperature of $T = 2$ K. When a current pulse is applied in the $+\mathbf{x}$ direction with an in-plane external assisting magnetic field B_x driving **m** toward $+\mathbf{x}$ direction, it gives $\mathbf{B}_{DL} = B_{DL}\,\mathbf{m} \times \boldsymbol{\zeta}$ a $-\mathbf{z}$ component to flip the magnetization from $+\mathbf{z}$ to $-\mathbf{z}$. This is only possible with $\boldsymbol{\zeta} = -\mathbf{y}$, which is the spin direction of the bottom surface state. Therefore, from the switching polarity, it is determined that the bottom surface states dominate the switching process.

Notably, the difference in the anomalous Hall resistance ΔR_{yx} switched by the current is as large as 9.2 kΩ, among the largest of all SOT systems. This is thanks to the large anomalous Hall resistance of 14.8 kΩ that Device No. 1 exhibits. The switching current density J_C is also as low as 4.5×10^5 A cm^{-2}, and the switching ratio of the magnetic domains is about 31%.

To further reduce the switching current density, Device No. 2, 6 QL $V_{0.14}(Bi_{0.18}Sb_{0.82})_{1.86}Te_3$ with a higher interfacial charge-to-spin conversion efficiency of 3.9 nm^{-1} (than Device No. 1's 2.0 nm^{-1}, which we will discuss later) is used. From Figure 2c, Device No. 2 shows a much lower switching current density of 2.8×10^5 than 4.5×10^5 A cm^{-2} in Device No. 1, which is almost 40% reduction and consistent with the increase of SOT efficiency. The switching current density is two orders of magnitude smaller than typical HMFM bilayers,[1,5,6,13,14] and on the same order of magnitude but slightly larger than that in Cr-doped $(Bi,Sb)_2Te_3$ (CBST) (≈2.57×10^5 A cm^{-2}) under the same pulse-driven switching scheme,[32] because VBST's large perpendicular magnetic anisotropy (PMA) as a hard ferromagnet creates an additional energy barrier for magnetization switching.

The switching ratio of the magnetic domains is not 100% because of inhomogeneous magnetic domains, so some earlier works on the switching of Cr-doped MTI show a switching ratio of <10%.[18,19,32] By enhancing the PMA of VBST with increased V doping, the switching ratio can be further improved to 60% (see Figure S9, Supporting Information).

To demonstrate how giant the switching of the Hall resistance in VBST is, a comparison between the switched resistances by current in various schemes is presented in Figure 2d. The changes in the anomalous Hall resistance by current-driven SOT switching are presented in HMFM systems including AlO_x/Pt/Co & Ta/CoFeB/MgO,[5,6] TI/MTI systems like Cr-doped $(Bi,Sb)_2Te_3$/$(Bi,Sb)_2Te_3$ (CBST/BST),[32,46] TI/magnetic insulator (MI) systems such as $Cr_2Ge_2Te_6$/$(Bi,Sb)_2Te_3$ (CGT/BST),[40] and V-doped $(Bi,Sb)_2Te_3$ (VBST, this work). For comparison, the change in the tunnel magnetoresistance (TMR) of the magnetic tunnel junction (MTJ) in IBM's spin-transfer torque (STT) MRAM is also listed here.[48] From the comparison, the giant switching of Hall resistance of 9.2 kΩ in VBST is almost four orders of magnitude higher than those in conventional HMFM systems[5,6] or TI/metallic FM systems (≈1 Ω),[34–36] making it among the largest of all SOT systems. The change of anomalous Hall resistance is even comparable to or greater than the change of TMR in MTJ devices, which makes the Hall channel a good readout and eliminates the need to fabricate complicated three-terminal SOT-MTJ structures.

In summary, the current-driven switching tests further establish VBST as an ideal spintronics material for its giant switched anomalous Hall resistance, larger switching ratio, and low critical switching current density due to its unique band topology, large anomalous Hall resistance, and highly efficient surface-state-mediated SOT.

4. Second-Harmonic Measurements of SOT Effective Fields

In order to determine either the DL or the FL SOT effective field B_{DL} and B_{FL} and thus the SOT efficiency in VBST, in-plane low-field second-harmonic measurements were conducted by applying either an external longitudinal or transverse magnetic field, B_L or B_T to slightly tilt the magnetization, as illustrated in Figure 2a. The first and second harmonic Hall voltages $V_{yx}^{1\omega}$ and $V_{yx}^{2\omega}$ were measured by lock-in amplifiers at the ambient temperature of $T = 2$ K with a sinusoidal excitation current of 10 μA (root mean square value). **Figure 3** presents one of the results of the $V_{yx}^{1\omega}$ and $V_{yx}^{2\omega}$ as a function of B_L in Device No. 2, 6 QL $V_{0.14}(Bi_{0.18}Sb_{0.82})_{1.86}Te_3$ when the magnetization was initialized to either $+\mathbf{z}$ or $-\mathbf{z}$ direction, revealing a parabolic dependence of $V_{yx}^{1\omega}$ and a linear dependence of $V_{yx}^{2\omega}$ on B_L, respectively. We can obtain the DL effective field B_{DL} from the data by Equation (2).[49,50]

$$B_{DL} = -2\frac{\partial V_{yx}^{2\omega}}{\partial B_L} \Big/ \frac{\partial^2 V_{yx}^{1\omega}}{\partial B_L^2} \tag{2}$$

By using the above equation, $B_{DL} = (2.59 \pm 0.20) \times 10^{-2}$ T. As an important indicator of the SOT efficiency, the DL SOT effective field to electric current density ratio is thus $B_{DL}/J = (1.56 \pm 0.12) \times 10^{-6}$ T A^{-1} cm^2, more than three orders of magnitude larger than typical HMFM bilayer heterostructures.[1,5,6,13,14] Here, the device parameters of a width of 10 μm and a thickness of 6 nm are used.

Another important indicator of SOT efficiency is the interfacial charge-to-spin conversion efficiency q_{ICS}, which is defined as the ratio of the 3D spin current density $J_{S,3D}$ to the 2D electric current density $J_{C,2D}$ as in Equation 3. This indicator applies to the 2D interfacial origin of SOT, like the Rashba–Edelstein Effect and TSSs.[6,20]

$$q_{ICS} = \frac{J_{S,3D}}{J_{C,2D}} = \frac{2eM_S B_{DL}}{\hbar J_{C,3D}} \tag{3}$$

here, M_S is the saturation magnetization and $J_{C,3D}$ is the 3D electric current density. This is a better metric than the spin Hall

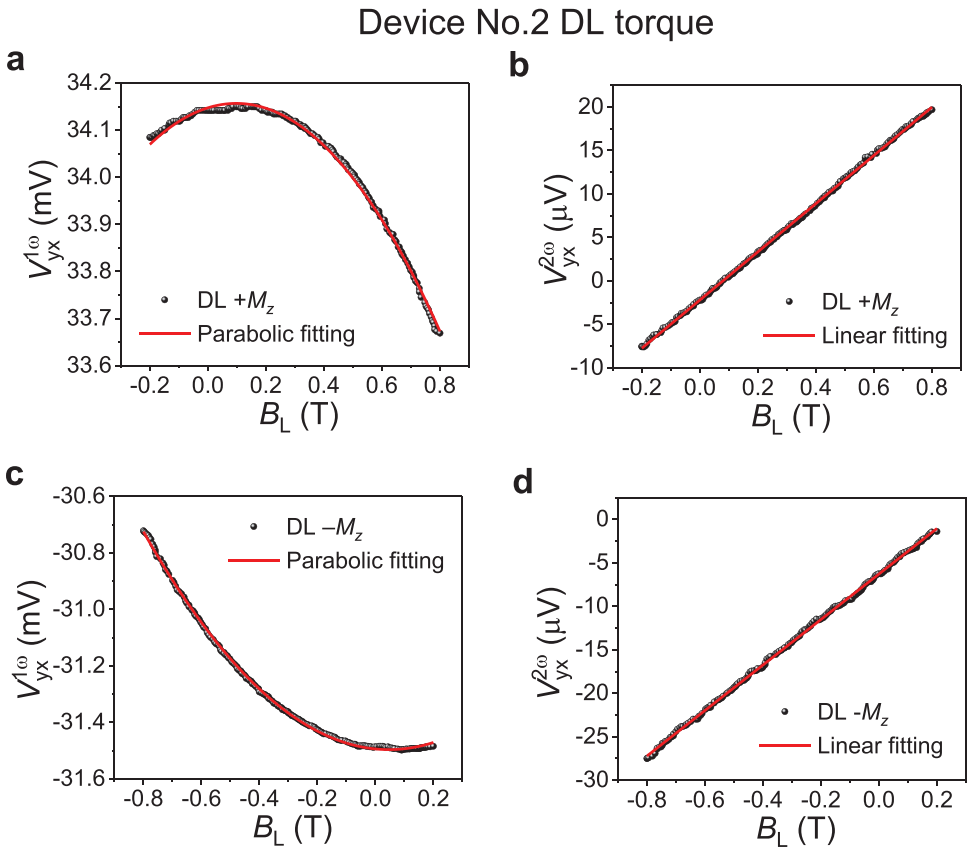

Figure 3. In-plane low-field second-harmonic measurements of the damping-like (DL) spin-orbit torque (SOT) effective field for Device No. 2. a) In-phase first-harmonic and b) out-of-phase second-harmonic Hall voltages $V_{yx}^{1\omega}$ and $V_{yx}^{2\omega}$ as a function of an external longitudinal magnetic field B_L when the magnetization is along the + **z** direction (+M_z). c) In-phase first-harmonic and d) out-of-phase second-harmonic Hall voltages when the magnetization is along the − **z** direction (−M_z). All measurements were carried out at $T = 2$ K by applying a sinusoidal current of 10 μA.

angle $\theta_{SH} = J_{S,3D} / J_{C,3D} = q_{ICS}\, t$, where t is the thickness, since it only applies to the 3D bulk origin of SOT (like the spin Hall effect) and might not be physically meaningful in MTI. The q_{ICS} of VBST in Device No. 2 is as large as 3.9 ± 0.3 nm^{-1}, indicating its high efficiency.[1,5,6,13,14]

Note that although this in-plane low-field second-harmonic method is subject to the artificial contributions from thermoelectric effects, such as the Nernst effect, such contributions are proved to be negligible by a different method of the angle-resolved second harmonic measurements in Section S11 (Supporting Information).[51] This in-plane low-field second-harmonic method also has a negligible contribution from the asymmetric magnon scattering reported by Yasuda et al.[46] because in order to have a sufficiently large contribution from the asymmetric magnon scattering, the magnetization has to be driven almost fully in plane by a large external field. However, in our method, with the large PMA of VBST and a small external field, only up to 1%–2% of the magnetization is driven in plane.

In short, the second-harmonic measurements further demonstrate the huge potential of VBST as an ideal spintronics material for its ultrahigh SOT efficiency, which arises from the spin-momentum-locked surface state and is free from interfacial or shunting problems in bilayers.

5. Fermi Level Dependence of SOT by Gate and Composition Tuning

5.1. Gate Tuning

In order to determine the SOT's dependence on Fermi level, 6 QL $V_{0.14}(Bi_{0.29}Sb_{0.71})_{1.86}Te_3$ was fabricated into a Hall bar with a top gate (Device No. 3). Notably, this device exhibits the QAHE at $T = 100$ mK (see Figure S3, Supporting Information) with chiral edge states in transport only, indicating that the Fermi level is within the exchange gap of the Dirac cone. By tuning the top gate voltage V_G from +6 to −6 V, the anomalous Hall resistance R_{yx} in **Figure 4a** shrinks from 20.8 to 16.0 kΩ at $T = 2$ K as the 2D hole density p increases from 3.79×10^{12} cm^{-2} to 4.51×10^{12} cm^{-2} at $T = 100$ K, indicating Fermi level is tuned lower and away from the Dirac point.[41,45] Here, 100 K is chosen for carrier density because only the ordinary Hall effect exists, and at 2 K, a large AHE makes the slope extraction inaccurate. Correspondingly in Figure 4b, the DL effective field to current density ratio B_{DL}/J increases from $(2.8 \pm 0.2) \times 10^{-7}$ to $(6.2 \pm 0.5) \times 10^{-7}$ T A^{-1} cm^2, and so does the interfacial charge-to-spin conversion efficiency q_{ICS} from 0.70 ± 0.03 to 1.5 ± 0.1 nm^{-1}, indicating an increase of the SOT efficiency.

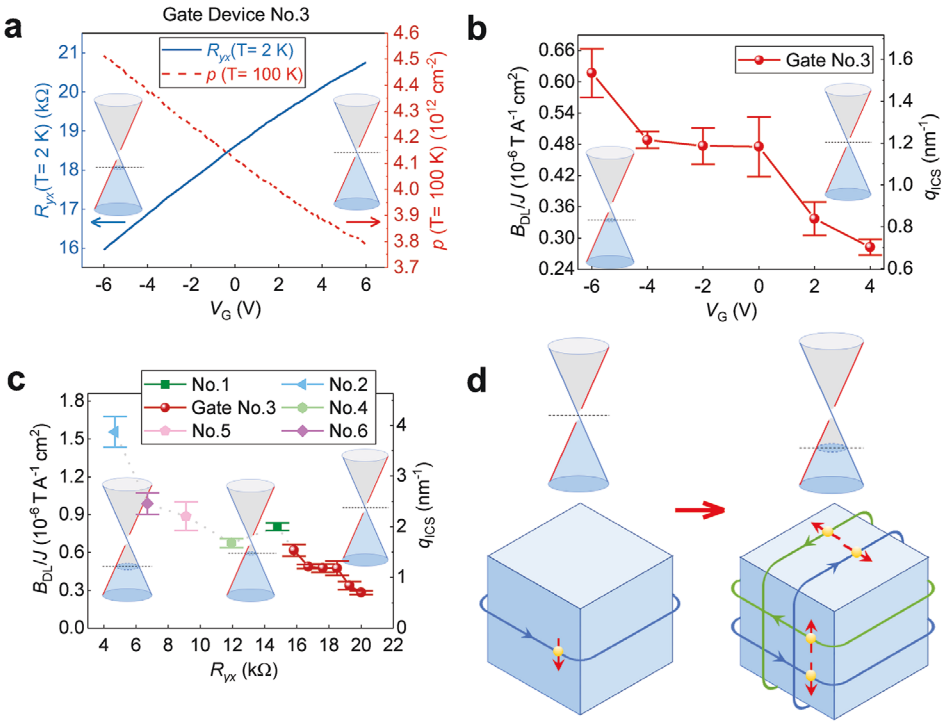

Figure 4. Electric field tuning and Fermi level dependence of V-doped $(Bi,Sb)_2Te_3$ (VBST) spin-orbit torque (SOT). a) Gate dependence of anomalous Hall resistance R_{yx} at $T = 2$ K and hole density p at 100 K in Device No. 3. b) Gate dependence of the SOT efficiency, as indicated by the damping-like (DL) effective field to current density ratio B_{DL}/J and the interfacial charge-to-spin conversion efficiency q_{ICS}, in Device No. 3. c) The dependence of the SOT efficiency on Fermi level, as indicated by the anomalous Hall resistance R_{yx} at 2 K in Device No. 1–6. The error bars in (b) and (c) represent the standard deviations from the measurements. d) A schematic showing the transition from the edge-state-dominated transport (when the Fermi level is in the exchange gap of the Dirac cone) to surface-state-dominated transport (when the Fermi level is away from the Dirac point).

5.2. Composition Tuning

In order to further tune the Fermi level beyond the range of electrostatic gating, more Hall bar devices of 6 QL $V_{0.14}(Bi_xSb_{1-x})_{1.86}Te_3$ (Device No. 1, 2, 4–6) were fabricated with a lower Bi level x than No.3 so that the Fermi level is tuned even lower and crosses the Dirac cone.[52] The details of each device are listed in **Table 1**, and the doping dependence of anomalous Hall resistance and hole density is presented in Figure S5 (Supporting Information). To compare with the gate tuning data, the anomalous Hall resistance R_{yx} at $T = 2$ K is used as a unifying indicator of the Fermi level because a smaller R_{yx} means a lower Fermi level.[41,45] As the R_{yx} is tuned to 4.69 kΩ in Figure 4c, the B_{DL}/J further increases to $(1.56 \pm 0.12) \times 10^{-6}$ T A^{-1} cm^2, and so does the q_{ICS} to 3.9 ± 0.3 nm^{-1} in Device No. 2, indicating an enhanced efficiency at lower Fermi level.

Both gate and composition tuning in VBST indicate that the SOT efficiency is significantly enhanced as the device transitions from the edge-state-dominated transport regime (with the Fermi level in the exchange gap) to the surface-state-dominated transport regime (with the Fermi level crossing the Dirac cone), as pictorially illustrated in Figure 4d. This confirms that the SOT in VBST is mediated by the top and bottom surface states. This is because the spin polarization of the edge state $\boldsymbol{\zeta} \| \mathbf{m}$ when $\mathbf{m}$ is aligned to the z direction, thus yielding $\mathbf{B}_{DL} = B_{DL}\, \mathbf{m} \times \boldsymbol{\zeta} = 0$, while the spin polarization of the top and bottom surface states $\boldsymbol{\zeta} \perp \mathbf{m}$, thus leading to a non-zero $\mathbf{B}_{DL}$.

Table 1. The composition of various devices.

Device no.	Bi level x	$R_{yx}(T = 2\ K)$ [kΩ]	B_{DL}/J [10^{-6} T A^{-1} cm^2]	q_{ICS} [nm^{-1}]
1	0.27	14.8	0.80 ± 0.03	2.0 ± 0.1
2	0.18	4.69	1.56±0.12	3.9 ± 0.3
3	0.29	16.0 to 20.8	0.62 ± 0.05 to 0.28 ± 0.02	1.5 ± 0.1 to 0.70 ± 0.03
4	0.24	11.95	0.68 ± 0.04	1.7 ± 0.1
5	0.22	9.11	0.89 ± 0.11	2.2 ± 0.3
6	0.20	6.70	0.99 ± 0.08	2.5 ± 0.2

Notably, this work's exploration in MTI's SOT during the transition from edge-state-dominated to surface-state-dominated transport regime is unique, since previous works of the gate tuning of SOT effective field in MTI or MTI/TI bilayer have only explored nonquantized surface-state-dominated transport regimes.[18,19,32,46]

6. Conclusion

In conclusion, we have explored SOT in a hard ferromagnetic TI thin film, V-doped $(Bi,Sb)_2Te_3$ (VBST). This material's large coercive field (>0.5 T) makes it robust against external magnetic disturbances, and its small magnetization (≈8.3 emu cm^{-3}) can minimize the stray field. We have demonstrated efficient SOT switching with a giant switched anomalous Hall resistance of 9.2 kΩ, among the largest of all SOT systems, thus making the Hall channel a good readout. The SOT switching current density can be as low as 2.8×10^5 A cm^{-2}, indicating ultrahigh efficiency, and the switching ratio can also be enhanced to 60%. By second-harmonic analysis, the SOT effective field to electric current density ratio can be as large as $(1.56 \pm 0.12) \times 10^{-6}$ T A^{-1} cm^2, and the interfacial charge-to-spin conversion efficiency can be as large as 3.9 ± 0.3 nm^{-1}, more than two orders of magnitude larger than those reported in heavy metal/ferromagnet (HMFM) bilayers. Fermi level dependence by both gate tuning and composition tuning indicates that the SOT in VBST is surface-state-mediated, so by tuning the Fermi level away from the Dirac point, more carriers from the surface states tend to enhance the SOT efficiency. This study confirms the potential of VBST as an ideal material candidate for the applications of energy-efficient magnetic memory devices, especially for cryogenic peripheral in-memory computing devices for quantum computing, which also requires low temperatures.[53]

7. Experimental Section

Growth of Materials: The V-doped $(Bi,Sb)_2Te_3$ (VBST) materials in this paper were grown on epi-ready semi-insulating GaAs (111)B substrates in an ultrahigh vacuum, Perkin–Elmer molecular beam epitaxy (MBE) system. Before growth, the substrates were loaded into the MBE chamber and pre-annealed at the temperature of 630 °C in a Te-rich environment to remove the oxide on the surface. During growth, high-purity Bi, Sb, and Te were evaporated from standard Knudsen cells, and V was evaporated from the Thermionics e-Gun electron beam evaporator. The substrate was kept at 180 °C. The reflection high-energy electron diffraction (RHEED) in situ was used to monitor the quality and thickness of the materials.

Material Characterizations: The HAADF–STEM characterization was performed on a 29 QL $V_{0.14}(Bi_{0.22}Sb_{0.78})_{1.86}Te_3$ thin film on a GaAs(111)B substrate with FEI Nova NanoLab 600 DualBeam (SEM/FIB). 0.5 mm Pt was first capped on top of the sample by electron beam-induced deposition to protect its surface. Then 1 µm Pt was deposited by ion beam-induced deposition. Finally, the sample was cleaned by 2 kV Ga ions with a low beam current of 29 pA and a small incident angle of 3° to minimize the damage. An FEI Titan 80–300 probe-corrected STEM/TEM microscope operating at 300 keV was used to capture HAADF–STEM images with atomic resolution.

The magnetization data were also taken on the same sample of 29 QL $V_{0.14}(Bi_{0.22}Sb_{0.78})_{1.86}Te_3$ by a superconducting quantum interference device (SQUID) magnetometer under VSM (vibrating sample magnetometer) mode and an out-of-plane geometry. The SQUID model is Quantum Design MPMS3 with a 7 T superconducting magnet, a base temperature of 1.8 K, and a sensitivity of 1×10^{-8} emu.

Device Fabrication: For all the devices (No. 1–8), the VBST thin films were fabricated into a 20 µm (length) × 10 µm (width) Hall bar geometry by a standard photolithography process. Cr/Au contact electrodes with thickness of 10/100 nm were deposited using an electron beam evaporator. For Device No. 3 only, an additional top gate was fabricated by exfoliating and transferring mica and graphite thin flakes on top to serve as the gate dielectric and the electrode, respectively.

Transport Measurements: Low-temperature magneto-transport measurements and current-induced switching tests were performed in a Quantum Design physical property measurement system (PPMS) with a 9 T superconducting magnet and a base temperature of 1.9 K. For magneto-transport measurements, a Keithley 6221 current source was used to generate a source AC current, and multiple lock-in amplifiers (Stanford Research SR830) were used to obtain the first and second-harmonic Hall voltages. For current-induced switching, a Keithley 2636 source meter was used to generate a series of writing and reading current pulses and to obtain the Hall voltages. Gate voltage was applied to the gate electrode of Device No. 3 and swept by a Keithley 2636 source meter.

Supporting Information

Supporting Information is available from the Wiley Online Library or from the author.

Acknowledgements

The authors acknowledge the support from the National Science Foundation (NSF) (DMR-1411085 and DMR-1810163) and the Army Research Office Multidisciplinary University Research Initiative (MURI) under grant numbers W911NF16-1-0472 and W911NF-19-S-0008. In addition, H.Z. acknowledges support from the U.S. Department of Commerce, NIST under financial assistance award 70NANB19H138. A.V.D. acknowledges support from the Material Genome Initiative funding allocated to NIST. F.X. acknowledges the support of the National Science Foundation under Grant No. OIA-2229498 and Oak Ridge Associated Universities Ralph E. Powe Junior Faculty Enhancement Award. J.L. acknowledges the support of the "Leading Talent" program of Shanghai and the National Natural Science Foundation of China (No. 12304089).

Conflict of Interest

The authors declare no conflict of interest.

Author Contributions

L.T., H.H., and S.K.C. contributed equally to this work. L.T., H.H., and K.L.W. conceived and designed the experiments. K.L.W. supervised the work. L.T., H.-Y.Y., T.-H.Y., X.D., and Y.R. grew the sample. H.Z. and A.V.D. performed the transmission electron microscopy measurement. L.T. performed the SQUID and XRD measurements. S.K.C. and Y.L. fabricated the Hall bar devices. L.T., H.H., and G.Q. carried out the transport measurements. L.T. processed all the data. All authors contributed to the analyses. L.T. and K.L.W. wrote the manuscript with contributions from all authors.

Data Availability Statement

The data that support the findings of this study are available from the corresponding author upon reasonable request.

Keywords

current-induced switching, hard ferromagnets, magnetic topological insulators, spin-orbit torque, topological surface states

Received: May 12, 2024
Revised: July 15, 2024
Published online: September 23, 2024

[1] A. Manchon, J. Železný, I. M. Miron, T. Jungwirth, J. Sinova, A. Thiaville, K. Garello, P. Gambardella, *Rev. Mod. Phys.* **2019**, *91*, 035004.
[2] J. E. Hirsch, *Phys. Rev. Lett.* **1999**, *83*, 1834.
[3] S. Zhang, *Phys. Rev. Lett.* **2000**, *85*, 393.
[4] Y. K. Kato, R. C. Myers, A. C. Gossard, D. D. Awschalom, *Science* **2004**, *306*, 1910.
[5] I. M. Miron, K. Garello, G. Gaudin, P. J. Zermatten, M. V. Costache, S. Auffret, S. Bandiera, B. Rodmacq, A. Schuhl, P. Gambardella, *Nature* **2011**, *476*, 189.
[6] L. Liu, C. Pai, Y. Li, H. W. Tseng, D. C. Ralph, R. A. Buhrman, *Science* **2012**, *336*, 555.
[7] Y. A. Bychkov, E. I. Rashba, *JETP Lett.* **1984**, *39*, 78.
[8] V. M. Edelstein, *Solid State Commun.* **1990**, *73*, 233.
[9] I. M. Miron, G. Gaudin, S. Auffret, B. Rodmacq, A. Schuhl, S. Pizzini, J. Vogel, P. Gambardella, *Nat. Mater.* **2010**, *9*, 230.
[10] D. Apalkov, B. Dieny, J. M. Slaughter, *Proc. IEEE* **2016**, *104*, 1796.
[11] N. Sato, F. Xue, R. M. White, C. Bi, S. X. Wang, *Nat. Electron.* **2018**, *1*, 508.
[12] M. Wang, W. Cai, D. Zhu, Z. Wang, J. Kan, Z. Zhao, K. Cao, Z. Wang, Y. Zhang, T. Zhang, C. Park, J. P. Wang, A. Fert, W. Zhao, *Nat. Electron.* **2018**, *1*, 582.
[13] L. Liu, O. J. Lee, T. J. Gudmundsen, D. C. Ralph, R. A. Buhrman, *Phys. Rev. Lett.* **2012**, *109*, 096602.
[14] G. Yu, P. Upadhyaya, Y. Fan, J. G. Alzate, W. Jiang, K. L. Wong, S. Takei, S. A. Bender, L. Te Chang, Y. Jiang, M. Lang, J. Tang, Y. Wang, Y. Tserkovnyak, P. K. Amiri, K. L. Wang, *Nat. Nanotechnol.* **2014**, *9*, 548.
[15] D. MacNeill, G. M. Stiehl, M. H. D. Guimaraes, R. A. Buhrman, J. Park, D. C. Ralph, *Nat. Phys.* **2017**, *13*, 300.
[16] Q. Shao, G. Yu, Y. W. Lan, Y. Shi, M. Y. Li, C. Zheng, X. Zhu, L. J. Li, P. K. Amiri, K. L. Wang, *Nano Lett.* **2016**, *16*, 7514.
[17] A. R. Mellnik, J. S. Lee, A. Richardella, J. L. Grab, P. J. Mintun, M. H. Fischer, A. Vaezi, A. Manchon, E. A. Kim, N. Samarth, D. C. Ralph, *Nature* **2014**, *511*, 449.
[18] Y. Fan, P. Upadhyaya, X. Kou, M. Lang, S. Takei, Z. Wang, J. Tang, L. He, L. Te Chang, M. Montazeri, G. Yu, W. Jiang, T. Nie, R. N. Schwartz, Y. Tserkovnyak, K. L. Wang, *Nat. Mater.* **2014**, *13*, 699.
[19] Y. Fan, X. Kou, P. Upadhyaya, Q. Shao, L. Pan, M. Lang, X. Che, J. Tang, M. Montazeri, K. Murata, L. Te Chang, M. Akyol, G. Yu, T. Nie, K. L. Wong, J. Liu, Y. Wang, Y. Tserkovnyak, K. L. Wang, *Nat. Nanotechnol.* **2016**, *11*, 352.
[20] K. Kondou, R. Yoshimi, A. Tsukazaki, Y. Fukuma, J. Matsuno, K. S. Takahashi, M. Kawasaki, Y. Tokura, Y. Otani, *Nat. Phys.* **2016**, *12*, 1027.
[21] C. L. Kane, E. J. Mele, *Phys. Rev. Lett.* **2005**, *95*, 146802.
[22] X. L. Qi, T. L. Hughes, S. C. Zhang, *Phys. Rev. B* **2008**, *78*, 195424.
[23] M. Z. Hasan, C. L. Kane, *Rev. Mod. Phys.* **2010**, *82*, 3045.
[24] Y. Chen, *Science* **2009**, *325*, 178.
[25] H. Zhang, C. X. Liu, X. L. Qi, X. Dai, Z. Fang, S. C. Zhang, *Nat. Phys.* **2009**, *5*, 438.
[26] F. Xiu, L. He, Y. Wang, L. Cheng, L. Te Chang, M. Lang, G. Huang, X. Kou, Y. Zhou, X. Jiang, Z. Chen, J. Zou, A. Shailos, K. L. Wang, *Nat. Nanotechnol.* **2011**, *6*, 216.
[27] Y. Wang, P. Deorani, K. Banerjee, N. Koirala, M. Brahlek, S. Oh, H. Yang, *Phys. Rev. Lett.* **2015**, *114*, 257202.
[28] Y. Wang, D. Zhu, Y. Wu, Y. Yang, J. Yu, R. Ramaswamy, R. Mishra, S. Shi, M. Elyasi, K. L. Teo, Y. Wu, H. Yang, *Nat. Commun.* **2017**, *8*, 1364.
[29] Y. Shiomi, K. Nomura, Y. Kajiwara, K. Eto, M. Novak, K. Segawa, Y. Ando, E. Saitoh, *Phys. Rev. Lett.* **2014**, *113*, 196601.
[30] H. He, L. Tai, H. Wu, D. Wu, A. Razavi, T. A. Gosavi, E. S. Walker, K. Oguz, C. C. Lin, K. Wong, Y. Liu, B. Dai, K. L. Wang, *Phys. Rev. B* **2021**, *104*, L220407.
[31] H. He, L. Tai, D. Wu, H. Wu, A. Razavi, K. Wong, Y. Liu, K. L. Wang, *APL Mater.* **2021**, *9*, 071104.
[32] X. Che, Q. Pan, B. Vareskic, J. Zou, L. Pan, P. Zhang, G. Yin, H. Wu, Q. Shao, P. Deng, K. L. Wang, *Adv. Mater.* **2020**, *32*, 1907661.
[33] Q. Shao, H. Wu, Q. Pan, P. Zhang, L. Pan, K. Wong, X. Che, K. L. Wang, *Int. Electron Devices Meet. IEDM* **2019**, *36*, 1.
[34] J. Han, A. Richardella, S. A. Siddiqui, J. Finley, N. Samarth, L. Liu, *Phys. Rev. Lett.* **2017**, *119*, 077702.
[35] H. Wu, P. Zhang, P. Deng, Q. Lan, Q. Pan, S. A. Razavi, X. Che, L. Huang, B. Dai, K. Wong, X. Han, K. L. Wang, *Phys. Rev. Lett.* **2019**, *123*, 207205.
[36] H. Wu, Y. Xu, P. Deng, Q. Pan, S. A. Razavi, K. Wong, L. Huang, B. Dai, Q. Shao, G. Yu, X. Han, J. C. Rojas-Sánchez, S. Mangin, K. L. Wang, *Adv. Mater.* **2019**, *31*, 1901681.
[37] N. H. D. Khang, Y. Ueda, P. N. Hai, *Nat. Mater.* **2018**, *17*, 808.
[38] M. Dc, R. Grassi, J. Y. Chen, M. Jamali, D. Reifsnyder Hickey, D. Zhang, Z. Zhao, H. Li, P. Quarterman, Y. Lv, M. Li, A. Manchon, K. A. Mkhoyan, T. Low, J. P. Wang, *Nat. Mater.* **2018**, *17*, 800.
[39] H. Wu, A. Chen, P. Zhang, H. He, J. Nance, C. Guo, J. Sasaki, T. Shirokura, P. N. Hai, B. Fang, S. A. Razavi, K. Wong, Y. Wen, Y. Ma, G. Yu, G. P. Carman, X. Han, X. Zhang, K. L. Wang, *Nat. Commun.* **2021**, *12*, 6251.
[40] M. Mogi, K. Yasuda, R. Fujimura, R. Yoshimi, N. Ogawa, A. Tsukazaki, M. Kawamura, K. S. Takahashi, M. Kawasaki, Y. Tokura, *Nat. Commun.* **2021**, *12*, 1404.
[41] C. Z. Chang, J. Zhang, X. Feng, J. Shen, Z. Zhang, M. Guo, K. Li, Y. Ou, P. Wei, L. L. Wang, Z. Q. Ji, Y. Feng, S. Ji, X. Chen, J. Jia, X. Dai, Z. Fang, S. C. Zhang, K. He, Y. Wang, L. Lu, X. C. Ma, Q. K. Xue, *Science* **2013**, *340*, 167.
[42] Y. Tokura, K. Yasuda, A. Tsukazaki, *Nat. Rev. Phys.* **2019**, *1*, 126.
[43] X. Kou, S. T. Guo, Y. Fan, L. Pan, M. Lang, Y. Jiang, Q. Shao, T. Nie, K. Murata, J. Tang, Y. Wang, L. He, T. K. Lee, W. L. Lee, K. L. Wang, *Phys. Rev. Lett.* **2014**, *113*, 137201.
[44] X. Kou, L. Pan, J. Wang, Y. Fan, E. S. Choi, W. L. Lee, T. Nie, K. Murata, Q. Shao, S. C. Zhang, K. L. Wang, *Nat. Commun.* **2015**, *6*, 8474.
[45] C. Z. Chang, W. Zhao, D. Y. Kim, H. Zhang, B. A. Assaf, D. Heiman, S. C. Zhang, C. Liu, M. H. W. Chan, J. S. Moodera, *Nat. Mater.* **2015**, *14*, 473.
[46] K. Yasuda, A. Tsukazaki, R. Yoshimi, K. Kondou, K. S. Takahashi, Y. Otani, M. Kawasaki, Y. Tokura, *Phys. Rev. Lett.* **2017**, *119*, 137204.
[47] L. He, X. Kou, M. Lang, E. S. Choi, Y. Jiang, T. Nie, W. Jiang, Y. Fan, Y. Wang, F. Xiu, K. L. Wang, *Sci. Rep.* **2013**, *3*, 3406.
[48] G. Hu, J. H. Lee, J. J. Nowak, J. Z. Sun, J. Harms, A. Annunziata, S. Brown, W. Chen, Y. H. Kim, G. Lauer, L. Liu, N. Marchack, S. Murthy, E. J. O'Sullivan, J. H. Park, M. Reuter, R. P. Robertazzi, P. L. Trouilloud, Y. Zhu, D. C. Worledge, *IEEE Int. Electron Devices Meet.* **2015**, 26.3.1.
[49] K. Garello, I. M. Miron, C. O. Avci, F. Freimuth, Y. Mokrousov, S. Blügel, S. Auffret, O. Boulle, G. Gaudin, P. Gambardella, *Nat. Nanotechnol.* **2013**, *8*, 587.
[50] J. Kim, J. Sinha, M. Hayashi, M. Yamanouchi, S. Fukami, T. Suzuki, S. Mitani, H. Ohno, *Nat. Mater.* **2013**, *12*, 240.
[51] H. Yang, H. Chen, M. Tang, S. Hu, X. Qiu, *Phys. Rev. B* **2020**, *102*, 024427.
[52] J. Zhang, C.-Z. Chang, Z. Zhang, J. Wen, X. Feng, K. Li, M. Liu, K. He, L. Wang, X. Chen, Q.-K. Xue, X. Ma, Y. Wang, *Nat. Commun.* **2011**, *2*, 574.
[53] Y. Liu, A. Lee, K. Qian, P. Zhang, H. He, Z. Ren, S. K. Cheung, Y. Li, X. Zhang, Z. Ma, Z. Xiao, G. Yu, X. Wang, J. Liu, Z. Wang, K. L. Wang, Q. Shao, (Preprint) arXiv: 2209.09443, v1, submitted: Septemeber, **2022**.